



Thermal blooming with laser-induced convection: radial basis function simulation

BENJAMIN F. AKERS,^{1,*} STEVEN T. FIORINO,² AND JONAH A. REEGER¹

¹Department of Mathematics and Statistics, Air Force Institute of Technology, WPAFB, Ohio 45433, USA

²Department of Engineering Physics, Air Force Institute of Technology, WPAFB, Ohio 45433, USA

*benjamin.akers@afit.edu

Received 19 February 2023; revised 24 April 2023; accepted 24 April 2023; posted 24 April 2023; published 22 May 2023

The propagation of a high energy laser through a nearly stagnant absorbing medium is studied. The absorption values and time scale of the problem are such that the laser induces convective heat currents transverse to the beam. These currents couple to the laser via the refractive index, causing time dependent thermal blooming. A numerical method is developed and applied to the model in [J. Electromagn. Waves Appl. 33, 96 (2019)], using radial basis functions for spatial differencing, which allows for irregular point spacings and a wide class of geometries. Both the beam and laser-induced fluid dynamics are numerically simulated. These simulations are compared to a historical experiment of a 300 W laser in a smoke-filled chamber with good agreement; both cases include a crescent shaped spot at the target.

<https://doi.org/10.1364/AO.487903>

1. INTRODUCTION

This study considers the propagation of a high energy laser through an absorbing fluid medium. In particular, we focus on a feedback mechanism between fluid heating and beam propagation known as thermal blooming [1,2]. Historical numerical simulations of thermal blooming simplify the motion of the fluid background by prescribing it [3–5], sampling it from a statistical distribution [6–8], or neglecting convection in the dynamics [9–12]. These numerical studies complement predictions of scaling laws and asymptotics [13–15] as well as experimental investigations [16,17]. As the thermal blooming phenomenon is one where fluid temperature dynamics play an important role, it is natural to simulate convection in the fluid. Recently, a model was proposed and simulated that includes fully nonlinear laser-induced fluid motions (due to temperature driven buoyancy changes) in fluids that are initially both uniform and quiescent [18–20]. (In this work, the Navier–Stokes equations are simulated directly, as compared to, for example, the approximate fluid flows used in [5,21].) Here, we compare the predictions of this model, to those of a laboratory experiment. We simulate the beam and fluid dynamics using a modern and novel numerical method, and discuss its performance as compared to the method in [18]. The current method is an improvement over a previous one in that it is flexible in its geometry and boundary conditions (where [18] requires square, periodic domains with equi-spaced points). Recent work in [19] suggests that resolving the exact physical domain becomes crucial for modeling steady state laser–fluid interactions; the numerical method described herein allows for the flexibility to simulate the model of [18] in realistic experimental geometries.

Both the laboratory experiment and numerical method consider a 300 W, 1.07 μm laser. The medium of propagation is a nearly quiescent smoke-filled aquarium. The beam travels 1 m, generating a 2 cm spot at a target board, whose dynamics are experimentally recorded. The experiment was conducted in 2010 by Peter Wick and Chris Lloyd, who kindly provided access to video of their trial for comparison purposes. The experiment is compared to numerical simulations of the beam spot through an initially quiescent fluid including the effect of convection. There are two major sources of discrepancy between experimental measurements and numerical results. First, the model does not include background fluid temperature or velocity fluctuations prior to turning on the laser, nor is it possible to prevent these completely experimentally. Second, both the real part of the refractive index and the linear loss rate for a smoke-filled aquarium are unknown and needed for the numerical simulations; estimated values are used. In spite of these difficulties, we observe good agreement between numerical simulations and the laboratory experiment.

2. MODELING

In this section, we present the mathematical system for the laser, a wave optics model, coupled with the Navier–Stokes equations for the fluid. This model was first presented in [18], where it was simulated using Fourier collocation in the extremely high power regime (the results of [18] in the geometry of this work would correspond to a MW class laser in clean dry air). In this work, a new numerical method is developed for this system, using radial basis functions (RBFs) [22]. The model is then simulated in

the 300 W power regime and compared to an experiment in a smoke-filled tank.

For beam propagation, we use the classic paraxial approximation to Maxwell's equations, which assumes only small deviations in refractive index and a separation of scales between the longitudinal and transverse aspect ratios of the laser. This model is well established in a number of communities as being accurate for the envelope of a traveling wave (see [23,24]):

$$\frac{\partial A}{\partial z} = \left(\frac{i}{2kn_0} \Delta_H - in_1k - \alpha \right) A, \quad (1)$$

where $k = 6 \times 10^4 \text{ cm}^{-1}$ is the wavenumber, A is the complex amplitude, Δ_H is the Laplacian in the coordinates transverse to the beam (here x and y), and parameter n_0 is the refractive index of the undisturbed medium at the particular laser wavelength [25].

The measurement of n_0 of an aerosol laden gas is complicated, and the range of realistic n_0 values is broad, and certainly depends on aerosol concentration. For example, the real part of the refractive index of cigarette smoke at 1070 nm is estimated at $n_0 \approx 1.5$ in [26], while clean air has a 1070 nm real refractive index of $n_0 \approx 1.00027$ [25]. The real index is defined as a measure of how much the speed of light is reduced from its vacuum value as it propagates through the medium. This propagation speed is largely determined by the number of molecules and other particles that light energy encounters during propagation (barring anomalous dispersion effects caused by strong absorption line effects, which are mostly absent around 1070 nm). Given that there are approximately 10^{22} gas molecules per ml (cm^3) of air, and at most about 10^6 aerosol particles per cm^3 in a cloud of cigarette smoke that could reduce visibility to hundreds of meters, the 16 orders of magnitude difference in the number concentration of molecules and particles indicates that the real index of smoky air is insignificantly different from clean air. We present simulations with both extremes, $n_0 = 1.0005$ (near the clean air value [25]) and $n_0 = 1.5$ (pure smoke [26]).

The refractive index correction n_1 is modeled using the Gladstone–Dale relationship for an ideal gas with density fluctuations coupled to temperature fluctuations via a Boussinesq approximation [18]:

$$n_1 = (n_0 - 1) \frac{\rho_1}{\rho_0}, \quad \frac{\rho_1}{\rho_0} = \frac{T_1}{T_0}, \quad n_1 = (n_0 - 1) \frac{T_1}{T_0}.$$

The linear loss rate, or extinction, α , is unknown, but an estimate of it can be quantified with a radiative transfer code such as LEEDR [27]. LEEDR can break down the gaseous molecular effects into scattering and absorption losses for propagation at any wavelength from the UV to the RF based on the latest spectroscopic databases (e.g. HITRAN 2016) coupled to a full or partial (Rayleigh where applicable) Mie scattering calculation. LEEDR also provides estimates of extinction losses due to suspended particulates or aerosols such as cigarette smoke through a comprehensive database of complex index of refraction optical properties, where the real part of the index dictates the speed of propagation (as described above), and the imaginary part captures the absorption magnitude. Assumed conditions of 22°C and 50% relative humidity with a particulate distribution representing 300 m visibility in a cloud of

cigarette smoke (the LEEDR calculation uses optical properties for a nearly equal mixture of soot and water soluble particles) yield a 1070 nm molecular extinction of $3.6 \times 10^{-3} \text{ km}^{-1}$ ($2.8 \times 10^{-3} \text{ km}^{-1}$ absorption plus $8 \times 10^{-4} \text{ km}^{-1}$ scattering) and aerosol extinction of 3.4 km^{-1} (2.8 km^{-1} scattering plus 0.6 km^{-1} absorption). Thus while the real index is dominated by the sheer number of gaseous molecules, the extinction is nearly all due to the relatively high concentration of smoke particulate.

The temperature fluctuations are evolved in the incompressible Navier–Stokes equations, presented in non-dimensional forms as

$$u_t + (u \cdot \nabla)u = \nabla P + \frac{1}{\text{Re}} \Delta u + \text{Ri} T \vec{e}_2, \quad (2a)$$

$$T_t + (u \cdot \nabla)T = \frac{1}{\text{Pe}} \Delta T + \text{St} |A|^2, \quad (2b)$$

$$\nabla \cdot u = 0. \quad (2c)$$

These equations have been non-dimensionalized using a beam width as the characteristic length scale L , velocity scale U , convective time scale $\tau = \frac{L}{U}$, temperature scale T_0 , beam intensity scale of A_0 , and pressure scale of $P_0 = \rho_0 U^2$. Variable T is normalized temperature fluctuations $T = \frac{T_1}{T_0}$; in Section 4, we report $T_1 = T_0 T$, so that our reported temperatures have more intuitive units, degrees K . The fluid length and velocity scales are measured against g , ν , and μ , the force due to gravity, the kinematic viscosity, and thermal diffusivity, respectively—typical choices in non-dimensional fluid simulations. The non-dimensional numbers introduced are the classic Reynolds (Re), Peclet (Pe), and Richardson (Ri), as well as the less common Stanton number (St) [28], defined as

$$\text{Re} = \frac{UL}{\nu}, \quad \text{Pe} = \frac{UL}{\mu}, \quad \text{Ri} = \frac{gL}{U^2}, \quad \text{St} = \frac{\beta A_0^2 L}{UT_0}.$$

These equations are valid for general values of the above parameters; the simulations presented here fix the values for a single experiment. We set $L = 2 \text{ cm}$, based on the beam spot diameter, $\tau = 0.1 \text{ sec}$, based on the experiment duration, $g = 981 \frac{\text{cm}}{\text{sec}^2}$, gravitational constant, and $U = 20 \frac{\text{cm}}{\text{sec}}$ from a convective scaling. Parameters $\rho = 1.2 \times 10^{-9} \frac{\text{kg}}{\text{cm}^3}$, $c_p = 1 \frac{\text{kJ}}{\text{kgK}}$, and $\nu = .15 \frac{\text{cm}^2}{\text{sec}}$, $\mu = 0.2 \frac{\text{cm}^2}{\text{sec}}$ correspond to dry air. The beam power scale $V_0^2 = 191 \frac{\text{W}}{\text{cm}^2}$ is derived from the total laser power using $P = \pi r^2 / 2 A_0^2$ [5]. The constant $\beta = \frac{\alpha}{\rho_0 c_p}$ can be recovered from the linear loss rate estimated here at $\alpha = 3 \times 10^{-5} \text{ cm}^{-1}$.

3. NUMERICAL METHOD

Approximate solutions to Eqs. (1) and (2) are computed by first approximating derivatives in the direction transverse to beam propagation using the RBF generated finite differences (RBF-FD) approach that has been popularized over the last 20 years [29–34]. RBF-FD approaches have been shown to be computationally efficient and effective at solving problems that

require nonuniform discretizations for resolving rapidly changing features in the solution to a partial differential equation (PDE). In particular, [29] details the successes of solving systems of PDEs in geophysics (with characters similar to those in the model presented here) utilizing RBF-FD. The illustrations [29] (and references therein) highlight the efficiency that can be achieved with RBF-FD (even on a standard workstation) when compared to industry standard computational codes. More recently, RBF-FD discretization of a nonlinear wave equation was compared to Fourier-split step (a standard method for wave optics) in [22].

The method begins by discretizing the domain, taking advantage of problem symmetries. Consider the domain $\mathbf{x} \in \Omega \subset \mathbb{R}^2$ in the transverse direction. Any \mathbf{x} in the domain can be expressed componentwise as $\mathbf{x} = [x \ y]^T$. When the initial conditions are symmetric about the line $x = 0$, the values of A , u , T , and P maintain this symmetry for all time and propagation distance. This can be used to reduce the computational domain to $\tilde{\Omega} = \{\mathbf{x} \in \Omega : x \geq 0\}$. The set is discretized by scattering node locations, $\mathcal{S}_N = \{\mathbf{x}_i\}_{i=1}^N$ across $\tilde{\Omega}$, and by defining a set of fictitious nodes:

$$\tilde{\mathcal{S}}_N = \left\{ \mathbf{x} \in \Omega : \begin{bmatrix} -1 & 0 \\ 0 & 1 \end{bmatrix} \mathbf{x} \in \mathcal{S}_N \text{ and } \begin{bmatrix} 1 \\ 0 \end{bmatrix}^T \mathbf{x} \neq 0 \right\}.$$

That is, $\tilde{\mathcal{S}}_N$ is the set of points with a nonzero x component from \mathcal{S}_N reflected about $x = 0$. For each point $\mathbf{x}_k \in \mathcal{S}_N$, define the sets $\mathcal{N}_k = \{\mathbf{x}_{k,j}\}_{j=1}^n$ to be the n points in $\mathcal{S}_N \cup \tilde{\mathcal{S}}_N$ nearest to \mathbf{x}_k . Then the action of the differential operators on A , T , P , and the components of u will be approximated at each \mathbf{x}_k by first constructing an RBF interpolant of the function, with interpolation points from the set \mathcal{N}_k , and then computing the action of the operators on the interpolant. The RBF interpolants used here utilize the polyharmonic spline RBF $\phi(r) = r^7$ and supplemental bivariate polynomials up to degree $m = 7$ (as in, e.g., [32–34]). If \mathcal{L} is a linear operator and $f : \mathbb{R}^2 \rightarrow \mathbb{R}$ is smooth, the action of \mathcal{L} on f is then given by a matrix multiplication, i.e.,

$$[\mathcal{L}f(\mathbf{x})|_{\mathbf{x}=\mathbf{x}_1} \ \mathcal{L}f(\mathbf{x})|_{\mathbf{x}=\mathbf{x}_2} \ \cdots \ \mathcal{L}f(\mathbf{x})|_{\mathbf{x}=\mathbf{x}_N}]^T \approx D\mathbf{f}, \quad (3)$$

where

$$\mathbf{f} = [f(\mathbf{x}_1) \ f(\mathbf{x}_2) \ \cdots \ f(\mathbf{x}_N)]^T. \quad (4)$$

The $N \times N$ matrix operators are sparse (with nN nonzero entries) as long as $n \ll N$ (the number of nearest neighbors is much less than the total number of points). They are also made smaller by leveraging problem symmetries about $x = 0$ when populating the matrices. When the operator \mathcal{L} acts on a function f that is even about $x = 0$, the entries of row k of the matrix operator are defined as

$$D_{ki}^{\text{even}} = \begin{cases} w_{k,j} & \text{if } \mathbf{x}_{k,j} \in \mathcal{S}_N \text{ and } \mathbf{x}_{k,j} = \mathbf{x}_i \\ w_{k,j} & \text{if } \mathbf{x}_{k,j} \in \tilde{\mathcal{S}}_N \text{ and } \begin{bmatrix} -1 & 0 \\ 0 & 1 \end{bmatrix} \mathbf{x}_{k,j} = \mathbf{x}_i \\ 0 & \text{otherwise} \end{cases}$$

Likewise, if f exhibits odd symmetry about $x = 0$, then row k of D has entries

$$D_{ki}^{\text{odd}} = \begin{cases} w_{k,j} & \text{if } \mathbf{x}_{k,j} \in \mathcal{S}_N \text{ and } \mathbf{x}_{k,j} = \mathbf{x}_i \\ -w_{k,j} & \text{if } \mathbf{x}_{k,j} \in \tilde{\mathcal{S}}_N \text{ and } \begin{bmatrix} -1 & 0 \\ 0 & 1 \end{bmatrix} \mathbf{x}_{k,j} = \mathbf{x}_i \\ 0 & \text{otherwise} \end{cases}$$

After approximating the differential operators in the transverse direction, Eq. (1) reduces to

$$\frac{d}{dz} \mathbf{A}(z, t) = \left(\frac{i}{2kn_0} D_{\Delta}^{\text{even}} - \alpha I \right) \mathbf{A}(z, t) - ik(\eta_0 - 1) \times \mathbf{T}(z, t) \odot \mathbf{A}(z, t), \quad (5)$$

and Eq. (2) can be written as

$$\begin{aligned} \frac{d}{dt} \mathbf{u}(z, t) = & - \left(\mathbf{u}(z, t) \odot \left(D_x^{\text{odd}} \mathbf{u}(z, t) \right) \right. \\ & \left. + \mathbf{v}(z, t) \odot \left(D_y^{\text{odd}} \mathbf{u}(z, t) \right) \right) \\ & + \cdots D_x^{\text{even}} \mathbf{P}(z, t) + \frac{1}{\text{Re}} D_{\Delta}^{\text{odd}} \mathbf{u}(z, t), \end{aligned} \quad (6a)$$

$$\begin{aligned} \frac{d}{dt} \mathbf{v}(z, t) = & - \left(\mathbf{u}(z, t) \odot \left(D_x^{\text{even}} \mathbf{v}(z, t) \right) \right. \\ & \left. + \mathbf{v}(z, t) \left(D_y^{\text{even}} \mathbf{v}(z, t) \right) \right) \\ & + \cdots D_y^{\text{even}} \mathbf{P}(z, t) + \frac{1}{\text{Re}} D_{\Delta}^{\text{even}} \mathbf{v}(z, t) + \text{RiT}(z, t), \end{aligned} \quad (6b)$$

$$\begin{aligned} \frac{d}{dt} \mathbf{T}(z, t) = & - \left(\mathbf{u}(z, t) \odot \left(D_x^{\text{even}} \mathbf{T}(z, t) \right) + \mathbf{v}(z, t) \odot \left(D_y^{\text{even}} \mathbf{T}(z, t) \right) \right) \\ & + \cdots \frac{1}{\text{Pe}} D_{\Delta}^{\text{even}} \mathbf{T}(z, t) + \text{StA}(z, t) \mathbf{1}. \end{aligned} \quad (6c)$$

System Eq. (6) uses the following discrete closure for the pressure, inherited from the continuous incompressibility condition:

$$\begin{aligned} D_{\Delta}^{\text{even}} \mathbf{P}(z, t) = & \left(D_x^{\text{odd}} \mathbf{u}(z, t) \right) \odot \left(D_x^{\text{odd}} \mathbf{u}(z, t) \right) \\ & + \mathbf{u}(z, t) \odot \left(D_{xx}^{\text{odd}} \mathbf{u}(z, t) \right) \\ & + \cdots \left(D_x^{\text{even}} \mathbf{v}(z, t) \right) \odot \left(D_y^{\text{odd}} \mathbf{u}(z, t) \right) \\ & + \mathbf{v}(z, t) \odot \left(D_{xy}^{\text{odd}} \mathbf{u}(z, t) \right) \\ & + \cdots \left(D_x^{\text{even}} \mathbf{v}(z, t) \right) \odot \left(D_y^{\text{odd}} \mathbf{u}(z, t) \right) \\ & + \mathbf{u}(z, t) \odot \left(D_{xy}^{\text{even}} \mathbf{v}(z, t) \right) \\ & + \cdots \left(D_y^{\text{even}} \mathbf{v}(z, t) \right) \odot \left(D_y^{\text{even}} \mathbf{v}(z, t) \right) \\ & + \mathbf{v}(z, t) \odot \left(D_{yy}^{\text{even}} \mathbf{v}(z, t) \right) - \text{Ri} D_y^{\text{even}} \mathbf{T}(z, t). \end{aligned}$$

In system Eq. (6) and Eq. (5), operators D_x , D_y , and D_Δ are the matrices that approximate the actions of $\frac{\partial}{\partial x}$, $\frac{\partial}{\partial y}$, and Δ , respectively. Here the operation \odot represents elementwise multiplication of two vectors, and \mathbf{u} , \mathbf{v} , \mathbf{T} , \mathbf{A} , and \mathbf{P} are defined using the notational convention of Eq. (4).

Variables T and u are slowly varying with respect to z and relative to x and y allowing for the independent evolution of system Eq. (6) at a discrete set of points in $\{z_i\}_{i=1}^{N_z}$. The present implementation solves system Eq. (6) at all values of z_i , $i = 1, 2, \dots, N_z$, with one call to MATLAB's ode113 with "RelTol" set to 10^{-3} and "AbsTol" set to 10^{-6} . At each intermediate time step of this adaptive Runge–Kutta method, the closure for $\mathbf{P}(z, t)$ must be solved as well as Eq. (5) for $\mathbf{A}(z, t)$. Equation (5) is also solved using MATLAB's ode113 with "RelTol" set to 10^{-3} and "AbsTol" set to 10^{-6} . Since this method is adaptive and requires a value of $\mathbf{T}(z, t)$ at each intermediate step in z , a cubic spline interpolant is constructed on the set $\mathbf{T}(z_i, t)$, $i = 1, 2, \dots, N_z$, and evaluated at the locations of z prescribed by the intermediate steps. In the present implementation, "free slip" boundary conditions are employed for the velocity. These conditions assume that at the boundary, the normal component of the velocity is zero, and that the normal derivative of the tangential component is zero. For example, if $\Omega = [-L, L] \times [-L, L]$, for $L > 0$, then at the right boundary, $u = 0$ and $\frac{\partial}{\partial x} v = 0$. For the pressure at the boundary,

$$\nabla P \cdot \mathbf{n} = (\mathbf{u} \cdot \nabla) \mathbf{u} \cdot \mathbf{n}$$

is enforced pointwise.

4. RESULTS AND DISCUSSION

In this section, we present the results of the numerical method, including comparison to the laboratory experiment.

A. Cost of the Numerical Method

Using an N point discretization, and n nearest neighbors to construct the RBF stencils, construction of each approximate differential operator requires $O(n^3 N)$ operations, with $n \ll N$. This construction is "embarrassingly parallel" since the weights for the approximate derivative at each node can be computed independently. While we did not perform tests on parallel scaling here, the results on the scaling presented in [33] applies. The differential operators are sparse, with $O(nN)$ nonzero entries, so that at each time step, application of these operators through multiplication requires at most $O(nN)$ operations. In cases where a system of linear equations must be solved, e.g., when recovering the pressure from its closure, a precomputed sparse LU factorization is utilized to reduce the cost of obtaining the solution of the system of equations to $O(nN)$. The propagation of the solution in time (and in the propagation direction, z , in the paraxial equation) is completed using MATLAB's adaptive multi-step method (ode113). These adaptive methods have cost that grows with the eigenvalues of the differential equation. In this problem, these eigenvalues grow when the refractive index n_0 , wavenumber k , or number of spatial points is increased,

leading to longer computational times. An example runtime is reported in Section 4.3.

B. Node Sets and Convergence

To begin, the domain in the transverse direction is taken to be $\Omega = \{\mathbf{x} \in \mathbb{R}^2 : \|\mathbf{x}\|_2 \leq \rho\}$, corresponding to a cylindrical tube of radius ρ . Set \mathcal{S}_N is constructed by first dividing Ω radially into n_r concentric circles where the innermost circle has radius 0—a single point—and the outermost has radius ρ . To determine these radii first choose \tilde{r}_j , $j = 1, 2, \dots, n_r$, to satisfy the conditions

$$\tilde{r}_j - \tilde{r}_{j-1} = R(\tilde{r}_j, h), \quad (7a)$$

$$\tilde{r}_1 = 0, \quad (7b)$$

$$\tilde{r}_{n_r-1} \leq \rho, \quad (7c)$$

$$\tilde{r}_{n_r} > \rho, \quad (7d)$$

where the function $R: \mathbb{R} \times \mathbb{R} \rightarrow \mathbb{R}$ defines a desired node density at a given radius depending on a desired (maximum) node spacing h . The solution to system Eq. (7) can be found by iteratively increasing n_r , starting at two, and solving Eqs. (7a) and (7b) of (7) until (7c) and (7d) are satisfied. The radii of the concentric circles are then defined to be $r_j = \frac{\tilde{r}_j}{\tilde{r}_{n_r}} \rho$. Since symmetry about $x = 0$ is leveraged, the concentric circle with radius r_j is parameterized by an angle $\theta \in [-\frac{\pi}{2}, \frac{\pi}{2}]$. Discrete values of θ are chosen on this circle so that for $l = 0, 1, 2, \dots, n_{\theta_j}$,

$$\theta_{jl} = -\frac{\pi}{2} + l \frac{\pi}{n_{\theta_j}},$$

where

$$n_{\theta_j} = \left\lceil \frac{\pi}{2 \sin^{-1} \left(\frac{r_j - r_{j-1}}{2r_j} \right)} \right\rceil,$$

ensuring that the points on the circle of radius r_j are equally spaced in the 2-norm with spacing roughly equal to the difference between r_j and r_{j-1} . Here $\lceil \cdot \rceil$ denotes the ceiling operation. On each concentric circle, we then define a set of points $X_j = \{\mathbf{x}_{jl}\}_{l=0}^{n_{\theta_j}}$, with $\mathbf{x}_{jl} = r_j [\cos \theta_{jl} \sin \theta_{jl}]^T$, and take $\mathcal{S}_N = \bigcup_{j=1}^{n_r} X_j$. Two such nodes sets are illustrated in the left two frames of Fig. 1 for different choices of R and with $h = 0.75$ and $\rho = 15$.

Since the method utilized for propagation in t and z is adaptive, solutions were computed for small t and z to assess convergence of the algorithm described in the previous section relative to the typical spacing between points in the transverse direction. Using the node generation method just described, with $h = 1.5$, $\rho = 15$, and $R(r, h) = h$, a nearly uniformly spaced set of nodes was generated, and the solution to Eq. (6) was computed at $z = 1$ and $t = 0.0001$ with the physical parameter choices given at the beginning of the next

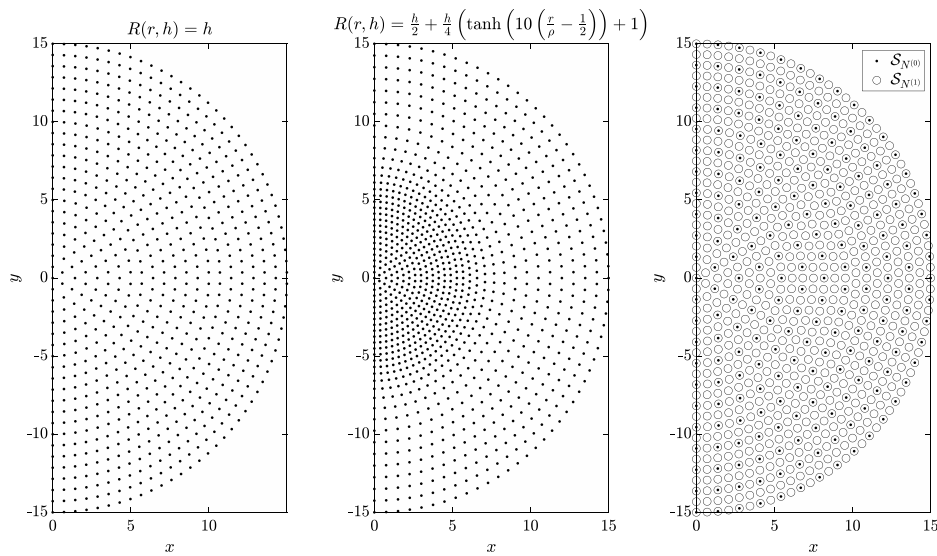


Fig. 1. Left two frames: two sets \mathcal{S}_N generated using the method described in Section 4 with $h = 0.75$, $\rho = 15$, and $R(r, h)$ as indicated. Right frame: first two node sets used for assessing convergence of the present algorithm with refinement in the transverse direction.

section. Parameter choices for the numerical method were $\phi(r) = r^7$, $m = 7$, $n = 90$. Denote the radii of the concentric circles generated in this initial case by $r_j^{(0)}$, $j = 1, 2, \dots, n_r^{(0)}$, and call the set of nodes generated $\mathcal{S}_{N^{(0)}}$. Let $p = 1, 2, \dots$, and from $\mathcal{S}_{N^{(0)}}$, new sets of radii are generated recursively such that $r_{2j}^{(p)} = \frac{r_j^{(p-1)} + r_{j+1}^{(p-1)}}{2}$, $j = 1, 2, \dots, n_r^{(p-1)} - 1$, and $r_{2j-1}^{(p)} = r_j^{(p-1)}$, $j = 1, 2, \dots, n_r^{(p)}$. The number of radii in each new set is then $n_r^{(p)} = 2n_r^{(p-1)} - 1$. Likewise, on the concentric circle of radius $r_{2j-1}^{(p)} = r_j^{(p-1)}$, the number relating to the discrete values of θ is increased so that $n_{\theta_j}^{(p)} = 2n_{\theta_j}^{(p-1)}$, and the values of the new angles are given by $\theta_{j(2l)}^{(p)} = \theta_{jl}^{(p-1)} = \frac{\pi}{2} + (2l) \frac{\pi}{n_{\theta_j}^{(p)}}$, $l = 0, 2, \dots, n_{\theta_j}^{(p-1)}$, and $\theta_{j(2l+1)}^{(p)} = \frac{\pi}{2} + (2l + 1) \frac{\pi}{n_{\theta_j}^{(p)}}$, $l = 0, 2, \dots, n_{\theta_j}^{(p-1)} - 1$. On the concentric circles of radius $r_{2j}^{(p)}$, those that do not correspond to radii in the set $\{r_j^{(p-1)}\}_{j=1}^{n_r^{(p-1)}}$, the discrete values of θ and resulting set $X_{2j}^{(p)}$ are defined as in the previous paragraph. Defining a set of nodes, $\mathcal{S}_{N^{(p)}}$, from these new radii and angles guarantees that it contains $\mathcal{S}_{N^{(p-1)}}$ while cutting the node spacing roughly in half. An illustration of $\mathcal{S}_{N^{(0)}}$ and $\mathcal{S}_{N^{(1)}}$ is given in the right frame of Fig. 1. After generating the node set $\mathcal{S}_{N^{(p)}}$, the solution to system Eq. (6) is again computed at $z = 1$ and $t = 0.0001$, and the absolute difference is computed at each point in both discretizations, $\mathcal{S}_{N^{(p-1)}} \cap \mathcal{S}_{N^{(p)}}$. The maximum of the difference in the solutions at the points in $\mathcal{S}_{N^{(p-1)}}$ at each iteration of this process is shown against the largest distance between a node and its nearest neighbor for each consecutive set $\mathcal{S}_{N^{(p)}}$. That is, Fig. 2 illustrates that the largest absolute difference in the solutions computed on sets $\mathcal{S}_{N^{(p-1)}}$ and $\mathcal{S}_{N^{(p)}}$ for points in $\mathcal{S}_{N^{(p-1)}} \cap \mathcal{S}_{N^{(p)}}$ is plotted against

$$h^{(p)} = \max_{\mathbf{x}_i \in \mathcal{S}_{N^{(p)}}} \min_{\substack{\mathbf{x} \in \mathcal{S}_{N^{(p)}} \\ \mathbf{x} \neq \mathbf{x}_i}} \|\mathbf{x} - \mathbf{x}_i\|_2.$$

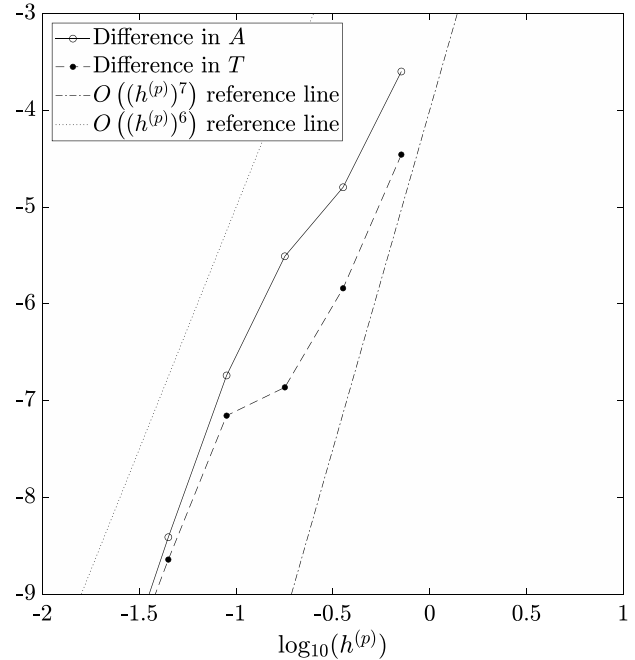


Fig. 2. Illustration of the convergence of the numerical method described in Section 3 relative to the typical spacing between nodes in the transverse direction to laser propagation. A convergence rate of roughly $O((h^{(p)})^7)$ is achieved, consistent with theoretical predictions.

The figure illustrates a convergence rate of $O((h^{(p)})^7)$, which corresponds to the choice of $m = 7$ and is consistent with the theoretical predictions in, for instance, [35].

C. Comparison of Simulation and Experiment

The numerical method described in Section 3 was applied with the parameter choices: $k = 5872.1358$, $\eta_0 = 1.0005$ and $\eta_0 = 1.5$, $\alpha = 3 \times 10^{-4}$, $St = 0.19$, $Ri = 981$,

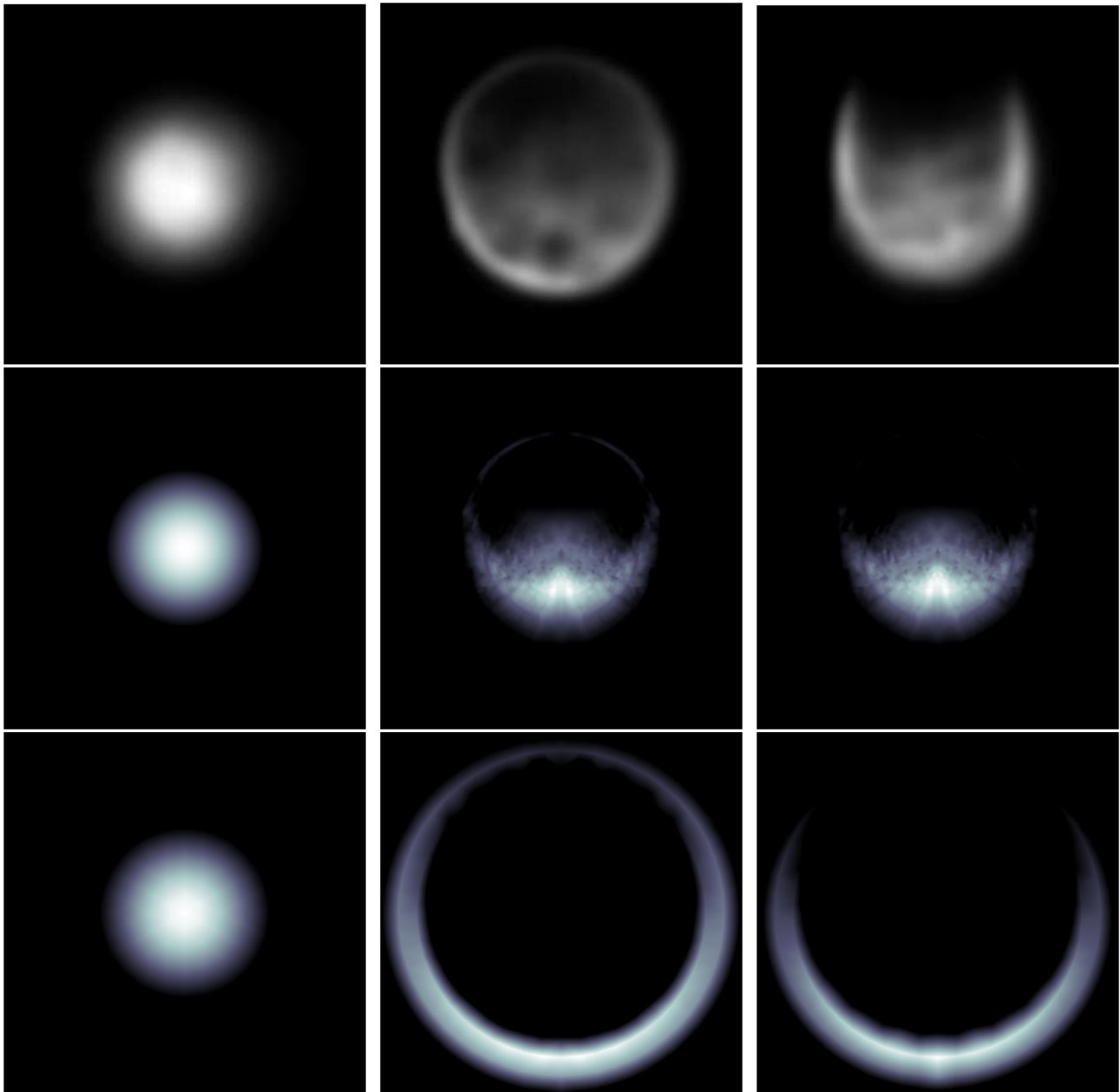


Fig. 3. Top row: photographs of the beam spot from the laboratory experiment at a sequence of times. Middle row: numerical simulations of the beam spot at estimated times ($t = 0, 0.4$, and 0.42) and distances ($z = 100$), with an estimated $\alpha = 0.0003$ and $\eta_0 = 1.0005$. Bottom row: numerical simulations of the beam spot at estimated times ($t = 0, 0.375$, and 0.46) and distances ($z = 100$), with an estimated $\alpha = 0.0003$ and $\eta_0 = 1.5$.

$Re = 6.67$, and $Pe = 5$. The node set used in the transverse direction was generated with node density based on $R(r, h) = \frac{h}{2} + \frac{h}{4}(\tanh(10(\frac{r}{\rho} - \frac{1}{2})) + 1)$, as in the center frame of Fig. 1, with $h = 0.1$ for $\eta_0 = 1.0005$ and $h = 0.05$ for $\eta_0 = 1.5$. Solutions are reported at $z = 100$, for both choices of η_0 , at three values of t and compared to the experiment in Fig. 3. Solutions were computed on a workstation with two Intel Xeon CPU E5-2697 v3 processors, each running at 2.60 GHz, and 256 GB of memory running MATLAB R2022b. The wall clock times required to compute the solutions for $\eta_0 = 1.0005$ and $\eta_0 = 1.5$ were roughly 41389 and 84927 s, respectively.

In Fig. 3, both the experimental measurements (top row) and numerical simulations (middle and bottom rows) experience laser-induced convective thermal blooming. All spots have increased in diameter and developed a crescent shape due to the buoyancy driven fluid flow (the crescent's orientation dictated by gravity). The numerical simulation begins with a perfectly quiescent atmosphere without temperature fluctuation. Neither of these is possible experimentally (small temperature fluctuations and velocity currents cannot be fully removed even in a closed tank). These initial fluctuations in the temperature and velocity account for some of the differences between the two figures (e.g., scintillation). The addition of the initial background

fluctuations to the simulation would require both changes to the numerical method (which interpolates the fluid parameters in the propagation direction) as well as a choice of initial fluctuations that were not measured experimentally. Additionally, we do not numerically simulate, nor model, the camera (so speckle and frame rate are additional sources of difference). We believe the framerate to be unimportant due to the time scale of the problem (if we numerically average our simulation over a framerate of 60 Hz, the pictures in Fig. 3 are not visibly different). Given that the absorption was not measured in the experiment, and no iterative refinement of the estimated value for α based on the output of the numerics was undertaken (nor do we think it makes sense to optimize α given the other sources of disagreement between the figures), we find the agreement between the figures to be excellent.

5. CONCLUSION

Numerical simulations of a high energy laser in an absorbing medium was presented. The parameter regime included laser-induced thermal blooming, with crescent formation. An RBF based spatial differencing method, which allows for irregular point spacings and a wide class of geometries, was developed and applied to the the laser–fluid model of [19]. Good agreement between experiment and numerical simulation was observed, given the limitations of the model equation.

Funding. Air Force Office of Scientific Research (Radial Basis Functions for Numerical Simulation); Office of Naval Research (APSHELs).

Acknowledgment. The authors thank Peter Wick and Chris Lloyd for access to the experimental data and helpful correspondence.

Disclaimer. This report was prepared as an account of work sponsored by an agency of the United States Government. Neither the United States Government nor any agency thereof, nor any of their employees, makes any warranty, express or implied, or assumes any legal liability or responsibility for the accuracy, completeness, or usefulness of any information, apparatus, product, or process disclosed, or represents that its use would not infringe privately owned rights. Reference herein to any specific commercial product, process, or service by trade name, trademark, manufacturer, or otherwise does not necessarily constitute or imply its endorsement, recommendation, or favoring by the United States Government or any agency thereof. The views and opinions of authors expressed herein do not necessarily state or reflect those of the United States Government or any agency thereof.

Disclosures. The authors declare no conflicts of interest.

Data availability. Data underlying the results presented in this paper are not publicly available at this time but may be obtained from the authors upon reasonable request.

REFERENCES

1. F. G. Gebhardt, "Twenty-five years of thermal blooming: an overview," *Proc. SPIE* **1221**, 2–25 (1990).
2. V. V. Vorob'ev, "Thermal blooming of laser beams in the atmosphere," *Prog. Quantum Electron.* **15**, 1–152 (1991).
3. L. C. Bradley and J. Herrmann, "Phase compensation for thermal blooming," *Appl. Opt.* **13**, 331–334 (1974).
4. F. G. Gebhardt, "Nonlinear propagation: thermal blooming," in *Atmospheric Propagation of Radiation* (1993), p. 288.
5. R. Karimzadeh, "Spatial self-phase modulation of a laser beam propagating through liquids with self-induced natural convection flow," *J. Opt.* **14**, 095701 (2012).
6. V. Banakh and A. Falits, "Numerical simulation of propagation of laser beams formed by multielement apertures in a turbulent atmosphere under thermal blooming," *Atmos. Oceanic Opt.* **26**, 455–465 (2013).
7. M. F. Spencer, I. V. Dragulin, D. S. Cargill, and M. J. Steinbock, "Digital holography wave-front sensing in the presence of strong atmospheric turbulence and thermal blooming," *Proc. SPIE* **9617**, 961705 (2015).
8. Y. Zhang, X. Ji, X. Li, and H. Yu, "Thermal blooming effect of laser beams propagating through seawater," *Opt. Express* **25**, 5861–5875 (2017).
9. J. N. Hayes, "Thermal blooming of laser beams in fluids," *Appl. Opt.* **11**, 455–461 (1972).
10. T. Karr, "Thermal blooming compensation instabilities," *J. Opt. Soc. Am. A* **6**, 1038–1048 (1989).
11. T. Karr, J. Morris, D. Chambers, J. Vieceilli, and P. Cramer, "Perturbation growth by thermal blooming in turbulence," *J. Opt. Soc. Am. B* **7**, 1103–1124 (1990).
12. S. Enguehard and B. Hatfield, "Perturbative approach to the small-scale physics of the interaction of thermal blooming and turbulence," *J. Opt. Soc. Am. A* **8**, 637–646 (1991).
13. Y. Huang and Y. Wang, "The scaling laws of laser beam spreading induced by turbulence and thermal blooming," *Proc. SPIE* **5639**, 65–69 (2004).
14. R. E. Kelly, I. Peter, and W. Shen, "Thermal blooming in axial pipe flow: the effects of beam shape and thermal conditions at the pipe wall," *Appl. Opt.* **19**, 3037–3039 (1980).
15. N. R. Van Zandt, S. T. Fiorino, and K. J. Keefer, "Enhanced, fast-running scaling law model of thermal blooming and turbulence effects on high energy laser propagation," *Opt. Express* **21**, 14789–14798 (2013).
16. R. Rohde and R. Buser, "Index of refraction turbulence effects on thermal blooming in laboratory experiments," *Appl. Opt.* **18**, 698–704 (1979).
17. R. O'Neil, H. Kleiman, and J. Lowder, "Observation of hydrodynamic effects on thermal blooming," *Appl. Phys. Lett.* **24**, 118–120 (1974).
18. B. F. Akers and J. A. Reeger, "Numerical simulation of thermal blooming with laser-induced convection," *J. Electromagn. Waves Appl.* **33**, 96–106 (2019).
19. J. Lane and B. Akers, "Numerical simulation of steady-state thermal blooming with natural convection," *Appl. Opt.* **62**, 2092–2099 (2023).
20. B. F. Akers and T. Liu, "Thermal effects in short laser pulses: suppression of wave collapse," *Wave Motion* **115**, 103079 (2022).
21. S. Reich, S. Schäffer, M. Lueck, M. Wickert, and J. Osterholz, "Continuous wave high-power laser propagation in water is affected by strong thermal lensing and thermal blooming already at short distances," *Sci. Rep.* **11**, 22619 (2021).
22. B. Akers, T. Liu, and J. Reeger, "A radial basis function finite difference scheme for the benjamin–ono equation," *Mathematics* **9**, 65 (2020).
23. C. Sulem and P.-L. Sulem, *The Nonlinear Schrödinger Equation: Self-focusing and Wave Collapse* (Springer, 2007), Vol. **139**.
24. J. Gustafsson, B. F. Akers, J. A. Reeger, and S. S. Sritharan, "Atmospheric propagation of high energy lasers," *Eng. Math. Lett.* **2019**, 7 (2019).
25. P. E. Ciddor, "Refractive index of air: new equations for the visible and near infrared," *Appl. Opt.* **35**, 1566–1573 (1996).
26. M. Yamasoe, Y. Kaufman, O. Dubovik, L. Remer, B. Holben, and P. Artaxo, "Retrieval of the real part of the refractive index of smoke particles from Sun/sky measurements during SCAR-B," *J. Geophys. Res. Atmos.* **103**, 31893–31902 (1998).
27. S. Fiorino, R. Randall, M. Via, and J. Burley, "Validation of a UV-to-RF high-spectral resolution atmospheric boundary layer characterization tool," *J. Appl. Meteorol. Climatol.* **53**, 136–156 (2014).
28. T. Cebeci and P. Bradshaw, *Physical and Computational Aspects of Convective Heat Transfer* (Springer, 2012).
29. B. Fornberg and N. Flyer, *A Primer on Radial Basis Functions with Applications to the Geosciences* (SIAM, 2015).

30. M. D. Buhmann, "New developments in the theory of radial basis function interpolation," in *Multivariate Approximation: From CAGD to Wavelets* (World Scientific, 1993), pp. 35–75.
31. J. A. Reeger, "Approximate integrals over the volume of the ball," *J. Sci. Comput.* **83**, 45 (2020).
32. J. A. Reeger, B. Fornberg, and M. L. Watts, "Numerical quadrature over smooth, closed surfaces," *Proc. R. Soc. London A* **472**, 20160401 (2016).
33. J. A. Reeger and B. Fornberg, "Numerical quadrature over the surface of a sphere," *Stud. Appl. Math.* **137**, 174–188 (2016).
34. J. A. Reeger and B. Fornberg, "Numerical quadrature over smooth surfaces with boundaries," *J. Comput. Phys.* **355**, 176–190 (2018).
35. V. Bayona, "An insight into RBF-FD approximations augmented with polynomials," *Comput. Math. Appl.* **77**, 2337–2353 (2019).